Oxidation state dependent conjugation controls electrocatalytic activity in a two-dimensional di-copper metal-organic framework

Anna Maria Dominic, [a] Zhiyong Wang,[a,f] Agnieszka Kuc,[b] Petko Petkov,[c] Khoa Hoang Ly,[a] Thi Lam Huong Pham,[d] Martin Kutzschbach,[d] Yuanyuan Cao,[e] Julien Bachmann,[e] Xinliang Feng,[a,f] Renhao Dong,[a] Inez M. Weidinger*[a]

Molecularly defined two dimensional conjugated metal-organic frameworks combine properties of molecular and material based electrocatalysts, enabling tunable active site and bandgap design. The rational optimization of these systems requires an understanding of the complex interplay between the various metal sites and their influence on catalysis. For this purpose, copper-phthalocyanine-based two-dimensional conjugated metal-organic framework (CuPc-CuO_4 2D c-MOF) films with an edge-on layer orientation were transferred to (Ni-NTA) functionalised graphite electrodes and analyzed via electrochemical resonance Raman spectroscopy. With the help of Density Functional Theory (DFT) calculations for the first time a detailed assignment of the vibrational bands for different Cu oxidation states could be achieved and correlated to their electrocatalytic activity in respect to the oxygen reduction reaction (ORR). Potential dependent Raman spectroscopy made it possible to determine the redox potentials of the Cu in the CuPc moieties and the Cu-catecholate nodes individually with E_{CuPc}= -0.04V and E_{CuO4}= +0.33 V vs. Ag|AgCl. Albeit the Cu-catecholates are generally seen as the active site in these systems, electrocatalytic ORR was only observed below -0.1 V were both Cu units were present in their respective Cu^{I} state. DFT calculations of bandgaps and density of states (DOS) showed a significant decrease in bandgap and increase in π-conjugation upon transition from the inactive mixed Cu^{II}/Cu^{I} state to the active Cu^{I}/Cu^{I} state suggesting that slow electron supply in the mixed state limits catalysis at the Cu-catecholates. Our results indicate that the coupling between metal oxidation changes and π-conjugation of the 2D c-MOF is a key parameter towards achieving good electrocatalytic activity.

Introduction

Electrochemical devices can be operated using renewable energy sources and thus have become the main alternative to devices that rely on fossil fuel combustion.[1] The need to use sustainable catalysts for the electrocatalytic key reactions, such as the reduction of oxygen and hydrogen, has led to enormous progress in the development of molecular and heterogeneous catalysts.[2–4] Specifically several carbon-based[5,6] and non-precious transition-metal[7–9] containing molecular complexes[10] have been developed that are capable of effectively catalysing ORR and other reduction reactions. A general problem for these molecular complexes remains the heterogenisation step. As intermolecular electron transfer rates are usually small, electroactive immobilisation above monolayer coverage is difficult to achieve.[11] As a result, the overall current densities are lower as in the case of heterogeneous catalysts that exhibit excellent intrinsic electric conductivity. [12,13] Materials that are synthesised via molecular bottom-up approaches have the ability to combine the precise active site design of molecular catalysts with the long range electron transfer capability of heterogeneous catalysts and have thus great potential towards improving electrode design beyond the state of the art.[14] Metal-organic frameworks (MOFs) use molecular units as building blocks to form high precision materials via coordination bonds between multidentate organic linkers and metal cations.[15] The high precision in material synthesis and extensive variability of building blocks allow them to be optimized for various applications such as gas storage, electronics and electrocatalysis.[16,17] Among them, two-dimensional conjugated MOFs (2D c-MOFs) that are based on metal phthalocyanines (MPcs) units, have shown excellent potential for electrocatalytic applications as they exhibit good ion diffusion ability and fully

[a.] *Technische Universität Dresden, Faculty of Chemistry and Food Chemistry, 01062 Dresden, Germany, inez.weidinger@tu-dresden.de*
[b.] *Helmholtz-Zentrum Dresden-Rossendorf, Abteilung Ressourcenökologie, Forschungsstelle Leipzig, Leipzig, Germany*
[c.] *University of Sofia, Faculty of Chemistry and Pharmacy, 1164 Sofia, Bulgaria*
[d.] *Institute of Ecology, Berlin University of Technology, Berlin, Germany*
[e.] *Friedrich-Alexander-Universität Erlangen-Nürnberg, Department of Chemistry and Pharmacy, Chemistry of thin films*
[f.] *Max Planck Institute for Microstructure Physics, Weinberg 2, Halle (Saale), D-06120 Germany*

Electronic Supplementary Information (ESI) available: UV vis spectra; Comparison of calculated and experimental Raman spectra; Blank LSV experiments and comparisons; Stability measurements during ORR; SEM images; Details of the ICP-MS (Inductively Coupled Plasma -Mass Spectrometry) measurements; RDE, K-L plots and determination of number of electrons involved in ORR; Additional Electrochemical Raman Spectra; Redox Titration of CuPc-$(OH)_8$ Monomer; Calculated spectra, bandgaps and DOS of different oxidation states ;All simulated systems are provided as cif files

in-plane π-delocalisation,[18,19] thereby overcoming the usually low conductivity of MOFs. Upon variation of the central metals, a large number of 2D c-MOFs have been developed recently that were specifically optimized for hydrogen evolution reaction (HER), oxygen reduction reaction (ORR) and carbon dioxide reduction reaction (CO_2RR).[20] In the case of ORR the metal-O_4 catecholates were identified as the active site for catalysis[21], yet the contribution of the MPc unit remained unclear.

For rational design of MOF electrocatalysts, a fundamental understanding of their redox and catalytic reaction mechanism is mandatory.[22] In-situ Raman spectroscopy is ideally suited to provide that information as it can be easily applied in an aqueous solution and under the influence of electric potential. Combining Raman spectroscopy with electrochemical data on the same system allows correlating electrocatalytic activity with structural changes of the material during catalysis and has been utilized to identify active sites and determine reaction mechanisms.[23–26] Specifically, in-situ Raman spectroscopy of iron phthalocyanines has been applied in the past to identify redox transitions and catalytic intermediates of these molecular units.[27–29] However, to the best of our knowledge, no Raman spectroelectrochemical work has been published yet on systems where the phthalocyanine was integrated into a MOF structure.

To get insight into the synergetic effects between the molecular building blocks in 2D c-MOFs, we have attached an edge-on layer oriented CuPc-based 2D c-MOF film with Cu-catecholates (CuPc-CuO_4)[30] via a Ni-NTA linker to a smooth graphite electrode. We were able to employ operando electrochemical resonance Raman spectroscopy to investigate the individual redox properties of the Cu species at the CuPc moieties and CuO_4 linkages and their respective contribution to the ORR. The experimental data was supported by theoretical Density Functional Theory (DFT) calculations of Cu^{I} and Cu^{II} oxidation states. Additionally, the bandgap energies and density of states (DOS) of the different states have been calculated to correlate the π-conjugation of the 2D c-MOF with the metal's oxidation states.

Results and Discussions

According to our previous report,[30] 2, 3, 9, 10, 16, 17, 23, 24 - octahydroxy phthalocyaninato Cu (CuPc-$(OH)_8$) monomer was employed as a ligand to construct the CuPc-CuO_4 2D c-MOF film on the water surface (Figure 1). The preferential edge-on orientation of the CuPc-CuO_4 film was determined by imaging and diffraction techniques.[30] The as-prepared film was transferred onto different solid substrates via dipping an electrode through the air-water interface.

In order to verify successful polymerisation and to elucidate structural differences between the (CuPc-$(OH)_8$) monomer and the CuPc-CuO_4 2D c-MOF, both complexes were attached to a roughened silver (Ag) electrode via dipping. Since the UV-vis spectra of CuPc-CuO_4 showed absorbance maxima at 320 nm and 620 nm (Figure S1), laser excitation at 595 nm was used that coincidences with the surface enhancement of the Ag electrode and the resonance Raman enhancement of CuPc-CuO_4.

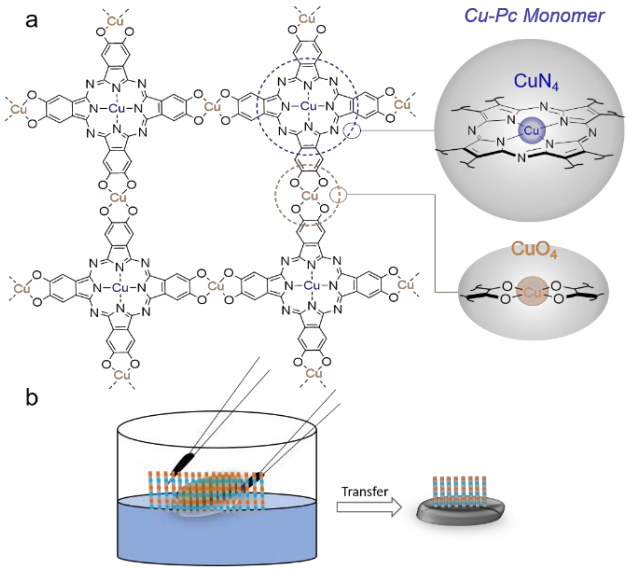

Figure 1 (a) Structure of CuPc-CuO_4, (b) Schematic illustration of the edge-on oriented CuPc-CuO_4 film on the water surface and transfer to solid electrodes.

This procedure allowed for a detailed analysis of the surface-attached CuPc-CuO_4 film via surface-enhanced resonance Raman spectroscopy (SERRS). The resulting SERR spectra at an electrode potential of 0.1 V vs. Ag|AgCl and are shown in Figure 2.

The spectral assignment was enabled by comparing the measured spectra with DFT calculations (Figure S2). Due to the enormous complexity of the spectral pattern, we will focus on the following selected bands that can be assigned confidently: Most importantly, a peak at 425 cm^{-1} rises in the CuPc-CuO_4 2D c-MOF that is absent in the calculated and measured spectra of the monomer. Two peaks at 402 and 464 cm^{-1} in the calculated CuPc-CuO_4 2D c-MOF spectrum can be assigned to this measured peak. Both represent out-of-plane vibrations that are only possible if a certain degree of polymerization has occurred. This makes them highly suitable marker bands to monitor the

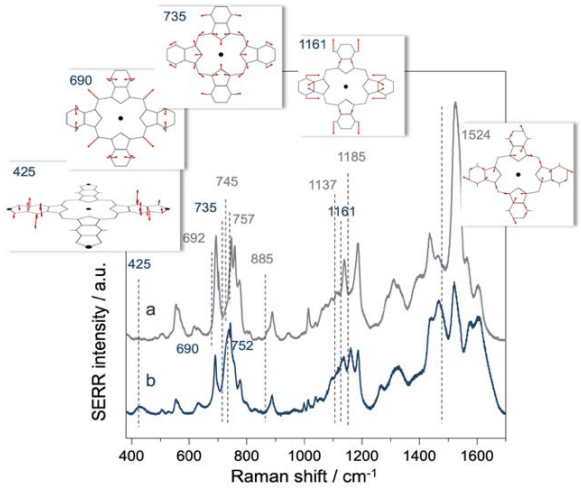

Figure 2. Surface-enhanced resonance Raman (SERR) spectra of the CuPc-$(OH)_8$ monomer (trace a) and the CuPc-CuO_4 MOF (trace b) at 0.1 V vs. Ag|AgCl (KCl 3M). Laser excitation: 595 nm. The insets illustrate the vibrations of selected vibrational modes as obtained from the DFT calculations.

polymerization process. Between 600 and 900 cm^{-1}, a prominent band occurs at 745 cm^{-1} in the monomer that is shifted to 735 cm^{-1} in the MOF. In comparison with DFT calculations we assign this band to a totally symmetric vibration at 777 cm^{-1} which includes both the Pc-unit and the phenol ligands but with a main contribution from the Pc (see inset Figure 2). A neighbouring band at 757 cm^{-1} can be seen in the monomer that is shifted to 752 cm^{-1} in the MOF, which is also assigned to vibration with a high contribution of the Pc. On the other hand, an isolated band at 887 cm^{-1} exists that does not shift upon polymerization. This band is also clearly present in the calculated spectra. Between 1000 and 1200 cm^{-1} two dominant bands at 1137 and 1185 cm^{-1} are seen in the monomer, whereas a third band at 1161 cm^{-1} is exhibited exclusively by the MOF. The shift to lower wavenumbers is confirmed in the calculations which predict a band-shift from 1173 to 1154 cm^{-1} in the monomer and MOF, respectively. We assign this band also to a combined Pc-phenol vibration, but in this case with a much higher contribution of the phenol rings and the CuO_4 linkages (see inset in Figure 2). Above 1200 cm^{-1}, a broad superposition of bands are seen that change in an unspecific manner upon polymerization. Also in this region, strong deviations between the calculated and measured spectra are observed. We, therefore, refrain from a more detailed assignment in this region. Note that the band at 1524 cm^{-1}, which is very dominant in the monomer, decreases significantly in intensity in the CuPc-CuO_4 2D c-MOF. The different modes are summarized in Table 1.

In a next step, ORR activity in O_2 saturated 0.1 KOH aqueous solution was tested by recording Linear Sweep Voltammetry (LSV) for the (CuPc-$(OH)_8$) monomer and the CuPc-CuO_4 2D c-MOF on a graphite electrode (Figure 3a). These experiments were performed in a hand-made spectroelectrochemical cell without rotation. The monomer (trace ii) showed some ORR activity below an onset potential of roughly -0.3 V vs. Ag|AgCl. Attaching the 2D c-MOF (trace iii) resulted in a steeper rise in catalytic current density, higher saturation currents and a shift of the onset potential to ca. -0.2 V vs. Ag|AgCl. In addition the corresponding Raman spectra of the CuPc-CuO_4 2D c-MOF on graphite were recorded. Since the surface enhancement is missing at these electrode interfaces, only a low-quality Raman spectrum could be detected (Figure 3b, trace iii).

Table 1. Selected experimental and corresponding calculated Raman frequencies of a CuPc-CuO_4 2D c-MOF in cm^{-1}

Labelling	Monomer exp.	Monomer calc.	MOF exp.	MOF calc.
ν_a	n.v.	n.v.	425	464
ν_b	692	713	690	709
ν_c	745	772	735	777
ν_d	757	792	752	799
ν_e	887	887	887	887
ν_f	1137	n.v.	1135	1131
ν_g	1185	1173	1161	1154
ν_h	1524	1515	1524	1495

The labelling of the modes (ν_a - ν_h) is done to simplify their discussion in the text; n.v.: not visible

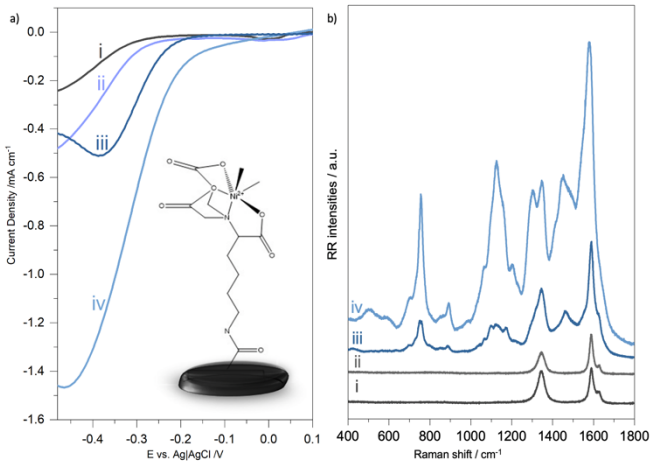

Figure 3. a) LSV curves in 0.1 M KOH in O_2 saturated atmosphere of (i) bare graphite electrode, (ii) CuPc-$(OH)_8$ Monomer on graphite electrode, (iii) CuPcCuO_4 MOF on graphite and (iv) CuPc-CuO_4 MOF on a Ni-NTA functionalized graphite electrode b) Raman Spectra of (i) bare graphite electrode, (ii) Ni-NTA functionalised blank graphite electrode, (iii) CuPc-CuO_4 MOF on graphite and (iv) CuPc-CuO_4 MOF on a Ni-NTA functionalized graphite electrode

To improve the adhesion, ORR current density and quality of the Raman spectra of the CuPc-CuO_4 2D c-MOF, the carbon electrode was functionalized with a nickel nitrilotriacetic acid (Ni-NTA) linker (Figure 3a inset) prior to the dipping process. Covalent attachment of the Ni-NTA to the carbon surface was achieved by running reduction and oxidation cycles in Ni (II) nitrate aqueous solution containing N_α, N_α-bis-(carboxymethyl)-L-lysin hydrate following published procedures.[31] For such modified graphite electrodes a significant increase of catalytic current (Figure 3a, trace iv) and Raman intensity of the CuPc-CuO_4 2D c-MOF (Figure 3b, trace iv) was observed. Also, the onset potential for ORR shifted to more positive potential and is now seen around -0.1 vs. Ag|AgCl. Note that the Ni-NTA alone did not yield any Raman signals or catalytic activity (Figure 3b trace ii and Figure S3). The stability and durability of the CuPc-CuO_4 2D c-MOF under catalytic conditions (-0.4 V) was proven by constant currents and identical Raman spectra before and after catalysis (Figure S4).

Scanning Electron Microscopy (SEM) images (Figure S5) showed an increased roughness of the Ni-NTA modified carbon surface after incubation pointing to a better attachment of the 2D c-MOF in this case. This was confirmed by Inductively Coupled Plasma -Mass Spectrometry (ICP-MS) measurements which yielded a Cu content of $0.6 \cdot 10^{-8}$ moles with and $0.06 \cdot 10^{-8}$ moles without prior Ni-NTA functionalization (for details see SI section 6). In the former case, an additional Ni content of $0.13 \cdot 10^{-8}$ M was measured. For the CuPc-CuO_4 Ni-NTA system catalytic currents were also recorded as a function of rotation frequency (Figure S6b) in an RDE setup. Although in this case the adhesion worked less good than in the spectroelectrochemical setup, corresponding Koutecky–Levich (KL) plots (Figure S6b inset) could be obtained at various electrode potentials that showed good linearity with an electron transfer number of 3.6 (See SI section 7).

The good quality of the Raman spectra of CuPc-CuO_4 on Ni-NTA modified graphite electrodes allowed performing Resonance Raman spectroelectrochemistry in the absence of oxygen. Here

we chose a close to neutral pH to guarantee maximal stability of the 2D c-MOF on the electrode. Figure 4a shows the in-situ Raman spectra recorded in 0.01 M H_2SO_4 under an inert atmosphere at different potentials (from 0.8 to -0.4 V *vs.* Ag|AgCl) in the frequency range from 400 to 1400 cm^{-1}. The spectrum resembles the one on Ag but with slightly shifted bands and lesser intensity. The peak at 425 cm^{-1} is barely visible but the peaks in the regions from 600 to 800 cm^{-1} and from 1100 to 1200 cm^{-1} are sufficiently intense to be analyzed. In the potential-dependent spectra, three species can be identified (Figure 4a). The same is true for the high-frequency range above 1400 cm^{-1} (Figure S7). Species III dominates at potentials above 0.4 V, in between 0.4 and -0.1 V, species II is rising whereas species I becomes dominant below -0.1 V. The rise and fall of these species can be most clearly seen in the band shifts in the region between 690 and 750 cm^{-1}, the relative intensities of which are plotted exemplarily in Figure 4b. The data could be fitted using the Nernst equation yielding two redox potentials of E_1 = 0.33±0.03 V and E_2 = -0.04±0.01 V, respectively.

In the following, we aim to assign the observed species I-III to their respective Cu/Cu oxidation states (in this notation the first Cu stands for the Pc-coordinated Cu ion and the second one for CuO_4 linkages). The CuPc under OCP conditions was determined recently to be present in its Cu^{II} oxidation state.[21] Redox titrations of selected bands of the CuPc-$(OH)_8$ monomer on rough Ag (Figure S8) showed a redox potential of the Cu^{II} → Cu^{I} transition to be at ca. -0.05 V vs. Ag|AgCl, which is close to our low potential redox transition at E_2=-0.04 V. We, therefore, assign species II to a Cu^{II}/Cu^{x} redox state, whereas species I refers to a Cu^{I}/Cu^{x} oxidation state.

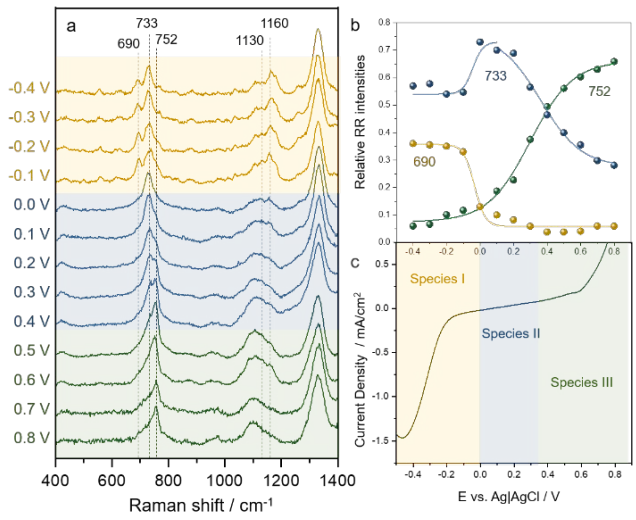

Figure 4. (a) Potential dependent Raman spectra of CuPc-CuO_4 on Ni-NTA modified graphite. Potentials are measured vs. Ag|AgCl reference electrode. (b) Analysis of peaks from 690 to 752 cm^{-1}. (c) LSV curve of CuPc-CuO_4 in O_2 saturated atmosphere in 0.1M KOH on Ni-NTA functionalized graphite electrodes.

For further assignment of both Cu oxidation states, Raman spectra were computed for Cu^{I}/Cu^{I}, Cu^{II}/Cu^{I} and Cu^{II}/Cu^{II} (See Table 2 and Figure S9, S10). For the Cu^{II}/Cu^{I} → Cu^{I}/Cu^{I} transition no significant change is observed for the ν_c marker band (789/791 cm^{-1}). We assign this band to the experimentally detected band at 733 cm^{-1} (ν_c). However, exclusively for species I, a vibration at 690 cm^{-1} (ν_b) occurs. Interestingly, theory predicts that this band should be present for all oxidation states with only minor shifts in frequency. However, in contrast to ν_c, the ν_b mode is highly polarization-dependent (Figure S11) and almost no contribution is expected for perpendicular polarization. We thus propose that the transformation into the Cu^{I}/Cu^{I} state goes hand in hand with a reversible re-orientation or scrambling of the preferential CuPc-CuO_4 2D c-MOF orientation. This interpretation is further supported by the observation of this band in other experimental setups, e.g., when adsorbed on rough Ag (see Figure 2) or in the presence of bound oxygen as shown in previous work.[21] For the Cu^{II}/Cu^{I} → Cu^{II}/Cu^{II} transition, calculations predict a redshift of the ν_c to 778 cm^{-1}, which is not seen a priori in the experimental data. However, the presence of the 733 cm^{-1} band even at very positive potential might account for this band (for simplicity, this peak area was fitted with three bands only). However, in the calculated spectra, the ν_d mode at 799 cm^{-1} is exclusively visible in the Cu^{II}/Cu^{II} state. Thus, we assign the band observed experimentally at 752 cm^{-1} to this mode.

The frequency region from 1100 to 1200 cm^{-1} shows distinct oxidation-dependent changes but due to the broad overlap, spectral analysis is very difficult and will be restricted to the previously assigned ν_f and ν_g modes (see Table 2). For the III → II transition only small changes are observed, whereas for the II → I transition more clearly defined peaks become visible but without any overall red- or blue-shift. Theory predicts no significant changes for the Cu^{II}/Cu^{II} → Cu^{II}/Cu^{I} transition, which supports our hypothesis that this is equivalent to the III → II transition. However, for the Cu^{I}/Cu^{I} state, a clear redshift is expected for the ν_g mode, which at first sight does not correlate with the experimental spectra. However, theory predicts a concomitant blueshift for the ν_f mode. Both effects combined would result in an overall non-visible peak shift in that spectral region as observed in the measured EC-Raman spectra. The assignment of oxidation-dependent Raman bands is summarized in Table 2. Based on the considerations discussed above we assign species III to the Cu^{II}/Cu^{II} state, species II to the Cu^{II}/Cu^{I} state and species I to the Cu^{I}/CuI state with the respective redox potentials of $E_{Cu(I)\rightarrow Cu(II)}$ = -0.04 V for the Cu in the Pc and $E_{Cu(I)\rightarrow Cu(II)}$ = 0.33V for Cu in the oxygen linkages.

The different redox transitions were subsequently compared with the obtained electrochemical currents in the same spectroelectrochemical cell and potential window (Figure 4 c). At potentials above 0.6 V vs. Ag|AgCl an oxidative current can be seen, which demonstrates the capability of this system to perform also the oxygen evolution reaction (OER). However, as the RR spectra did not show the same stability as for ORR, OER catalysis will not be considered in the present work. The observed onset potential for ORR around -0.1 V vs. Ag|AgCl, is close to the redox potential of the CuPc unit but far below the

Table 2. Selected Raman vibrations in cm^{-1} and bandgap energies in eV for the different Cu oxidation states

Bandgap energies obtained at HSE06 level of theory; n.v: not visible ; n.d: not determined

	Raman vibrations in cm^{-1}					
	Cu^{II}/Cu^{II}		Cu^{II}/Cu^{I}		Cu^{I}/Cu^{I}	
	exp.	calc.	exp.	calc.	exp.	calc.
ν_b	n.v.	709	n.v.	706	690	702
ν_c	733	778	733	789	733	791
ν_d	752	799	n.d.		n.d.	
ν_f	1129	1131	1126	1136	1157	1142
ν_g	1160	1154	1154	1155	1133	1120
	Bandgap in eV					
		0.92		1.25		0.51

redox potential of the Cu in the oxygen linkages. It is therefore concluded that ORR catalysis is only possible if both Cu-units are in their respective Cu^{I} state. This is per se not surprising as ORR in Cu based molecular complexes usually occurs from the Cu^{I} oxidation state.[32] More surprising is the observation that the Cu in the oxygen linkages, previously identified as an active site for oxygen reduction,[21] is unable to generate catalytic currents in the mixed state where the Cu in the Pc unit is still in its Cu^{II} state. An explanation for this can be derived by considering the bandgaps calculated for the 2D c-MOF in its different oxidation states (see Table 2 and Figure S12). Interestingly, the mixed-

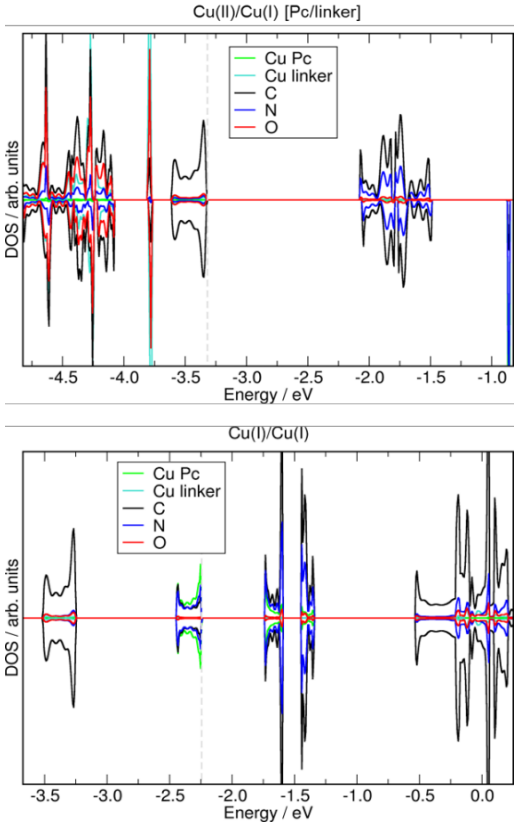

Figure 5. Density of states projected on atom types for the Cu^{II}/Cu^{I} (top) and Cu^{I}/Cu^{I} states (bottom). The dashed lines represent the Fermi level, set at the top of valence band.

state (Cu^{II}/Cu^{I}) has the highest bandgap of 1.25 eV, whereas the Cu^{I}/Cu^{I} state exhibits a significantly reduced bandgap of 0.51 eV. Additional calculations of DOS (Figure 5 and Figure S13) projected on atom types reveal a contribution of Cu (from Pc units), C and N atoms in the frontier orbitals in the Cu^{I}/Cu^{I} state, but almost only of C atoms in the Cu^{II}/Cu^{I} state. Cu states in Cu^{II}/Cu^{I} are situated at least 0.5 eV below the Fermi energy level and 2.5 eV above it. These calculations suggest that fast electron transport between the active Cu sites is only possible in the Cu^{I}/Cu^{I} state and not in the Cu^{II}/Cu^{I} state. This scenario suggests that the CuPc is not a catalytic site for ORR, but it needs to be present in its Cu^{I} state to enable fast electron supply for the ORR. The proposed reaction mechanism is summarized in Figure 6.

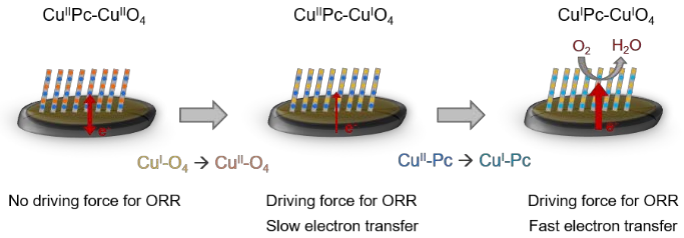

Figure 6. Proposed reaction mechanism based on the spectroelectrochemical data and calculations.

Materials and Methods

$CuPc\text{-}CuO_4$ MOF Synthesis: 200 µL of freshly prepared solution of $CuPc\text{-}(OH)_8$ in chloroform/DMF (2:1 in volume) (1 mg ml^{-1}) was spread onto the water surface in a beaker under ambient conditions. A green film was formed after 30 mins on the water surface due to the self-assembly of $CuPc\text{-}(OH)_8$. Coordination polymerization was achieved by the addition of an aqueous solution of copper(II) acetate (5 ml, 1mg ml^{-1}) and sodium acetate (2 ml, 1 mg ml^{-1}) into the water subphase. After 18h, $CuPc\text{-}CuO_4$ 2D c-MOF was obtained as translucent black thin films on the water surface which can be easily transferred to the electrodes.

Ni-NTA Modification of electrodes: A graphite disk electrode (1.2 cm in diameter) was first polished with alumina slurries (0.5 and 0.06 mm) and cleaned by sonication in Milli-Q water. After being cleaned with Milli-Q water, the electrode was immersed in 0.5 M sulfuric acid and scanned between 1 V and 1 V for 400 cycles at 200 mV s^{-1}. NTA–Ni^{2+} and NTA-Cu^{2+} then modified on the electrode surface by the cycling of GC electrode in 2 mM NTA–Ni^{2+} and NTA-Cu^{2+} solution between 500 mV and 1500 mV for about 200 scans at 200 mV s^{-1}. Following this, the interfacially synthesized CuPcCu MOFs are transferred to the modified electrode by dipping. The disc electrode, as the working electrode, was placed in a custom-made electrochemical cell, a platinum wire and an Ag/AgCl electrode were used as counter and reference electrodes respectively. Electrochemical experiments were conducted using an Ivium Vertex One EIS potentiostat with Ivium electrochemical software. Experiments were performed in 0.1 M KOH solution.

During LSV measurements for ORR, the sealed electrochemical cell was under continuous O_2 gas supply.

Resonance Raman spectroscopy was conducted using a confocal Raman microscope (S&I Monovista CRS+) with laser excitation by a Cobolt Mambo 594 nm diode laser. The laser was aligned and then focused on the sample using an Olympus 20× objective at a laser power of ≈1 mW. The sample stage was constantly moved during the measurement to avoid degradation. Spectra were calibrated with respect to the Raman spectrum of toluene. During the measurements, the cell was completely sealed, and a continuous flow of Ar gas was ensured.All systems were fully optimized using the Vienna ab-initio Simulation Package (VASP).[33] The electronic wavefunctions were expanded in a planewave basis set with a kinetic energy cutoff of 400 eV. The energy stopping criterion was set to EDIFF = 1E-6 eV. The geometry optimization convergence was set to forces acting on the ions that were smaller than 0.03 eV $Å^{-1}$. Electron-ion interactions were described using the projector augmented wave (PAW) method. [34] Generalized gradient approximation (GGA) of the exchange-correlation energy in the form of Perdew-Burke-Ernzerhof (PBE)[35] was applied together with Grimme D2 dispersion correction.[36] We used the DFT+U
approach to describe the localized d-orbitals of Cu ions. The effective Coulomb (U) and exchange (J) terms were set to 4 and 1 eV, respectively.[37] Such a combination of U and J was already successfully applied for very similar systems.[38] Monkhorst-Pack[39] Γ-centered grid with 2×2×4 dimension was used for K-point sampling of the Brillouin zone during the geometry optimization procedure. Different Cu oxidation states were obtained by the introduction of Na cations into the lattice close to the Cu nodes.
Electronic band structures and densities of states were calculated on the VASP optimized systems using Crystal17 software.[40,41] For Raman simulations, atomic positions were reoptimized using PBE0 functional[42] and Grimme D3 dispersion correction.[43]Band structures were calculated using HSE06 functional. [44] Monkhorst-Pack Γ-centered grid with 3×3×18 dimension was used together with POB-TZVP basis set for all atoms.[45]

Conclusions

In conclusion, we have for the first time attached CuPc-CuO_4 2D c-MOFs to a Ni-NTA functionalized graphite electrode, which enabled us to measure electrochemical Raman spectra of the CuPc-CuO_4 2D c-MOF on graphite as a function of applied potential. Comparison with calculated spectra allowed to determine the redox potentials of the $Cu^{II} \rightarrow Cu^{I}$ transition in the CuPc and the CuO_4 linkages to be E_{CuPc}= -0.04V and E_{CuO4}= 0.33 V respectively. We demonstrated that electrocatalytic ORR can only proceed when both units exist in their respective Cu^{I} oxidation state albeit catalytic activity would only require the $Cu^{II} \rightarrow Cu^{I}$ transition of the CuO_4 linkages. We rationalize this observation by the calculated low π-conjugation in the mixed Cu^{II}/Cu^{I} state that prevents fast electron supply to the active site. Reduction of the CuPc site significantly increases π-conjugation of the 2D c-MOF and enables the system to perform catalysis. Furthermore, the data suggest a change in orientation or scrambling of the CuPc-CuO_4 2D c-MOF in the catalytically active Cu^{I}/Cu^{I} state. Whether this effect is beneficial for catalysis e.g., by promoting oxygen diffusion into the layers must be further examined in the future. Our results demonstrate that the oxidation dependent conjugation of 2D c-MOFs has to be considered to further advance bimetallic MOFs in electrocatalysis.

Author Contributions

A.M.D, K.H.L. and I.M.W. performed the spectro-electrochemical measurements and data analysis. A.K. and P.P. performed DFT calculations and analysis. Z.W., X.F. and R.D. synthesized the MOFs. T.L.H.P., M.K., Y.C and J.B. contributed in characterizing the samples. The manuscript was written through contributions of all authors. All authors have given approval to the final version of the manuscript.

Conflicts of interest

There are no conflicts to declare.

Acknowledgements

The authors acknowledge financial support from the German Research Foundation (CRC1415 (417590517)), BA 4277/11-1 and EXC 2008/1 (UniSysCat) -390540038).
A.K. and P.P. acknowledge the GWK support for funding this project by providing computing time through the Center for Information Services and HPC (ZIH) at TU Dresden.

References

1 S. Chu and A. Majumdar, *Nature*, 2012, **488**, 294–303.
2 S. Dey, B. Mondal, S. Chatterjee, A. Rana, S. Amanullah and A. Dey, *Nat Rev Chem*, 2017, **1**, 0098.
3 D.D. Qin, Y. Tang, G. Ma, L. Qin, C.-L. Tao, X. Zhang and Z. Tang, *Int J Hydrogen Energy*, 2021, **46**, 25771–25781.
4 Z. Liang, H. Guo, G. Zhou, K. Guo, B. Wang, H. Lei, W. Zhang, H. Zheng, U.-P. Apfel and R. Cao, *Angewandte Chemie International Edition*, 2021, **60**, 8472–8476.
5 J. Wu, B. Liu, X. Fan, J. Ding, X. Han, Y. Deng, W. Hu and C. Zhong, *Carbon Energy*, 2020, **2**, 370–386.
6 Y. Qin, Z. Ou, C. Xu, Z. Zhang, J. Yi, Y. Jiang, J. Wu, C. Guo, Y. Si and T. Zhao, *Nanoscale Res Lett*, 2021, **16**, 92.
7 J. Pan, X. L. Tian, S. Zaman, Z. Dong, H. Liu, H. S. Park and B. Y. Xia, *Batter Supercaps*, 2019, **2**, 336–347.
8 J. Wang, H. Hu, H. Zhang, J. Zhao, X. Li, Z. Song, J. Ding, Y. Deng, X. Han and W. Hu, *Energy and Fuels*, 2021, **35**, 6483–6503.
9 Y. He, S. Liu, C. Priest, Q. Shi and G. Wu, *Chem. Soc. Rev*, 2020, **49**, 3484.
10 M. L. Pegis, C. F. Wise, D. J. Martin and J. M. Mayer, *Chem Rev*, 2018, **118**, 2340–2391.
11 C. Costentin, M. Robert and J.-M. Savéant, *Curr Opin Electrochem*, 2017, **2**, 26–31.
12 A. Corma, *Catalysis Reviews*, 2004, **46**, 369–417.

13 X. Cui, W. Li, P. Ryabchuk, K. Junge and M. Beller, *Nat Catal*, 2018, **1**, 385–397.
14 I. Luz, F. X. Llabrés i Xamena and A. Corma, *J Catal*, 2012, **285**, 285–291.
15 H. Furukawa, K. E. Cordova, M. O'Keeffe and O. M. Yaghi, *Science (1979)*, 2013, **341**, 1230444.
16 M. Wang, R. Dong and X. Feng, *Chem Soc Rev*, 2021, **50**, 2764–2793.
17 I. Liberman, R. Shimoni, R. Ifraemov, I. Rozenberg, C. Singh and I. Hod, *J Am Chem Soc*, 2020, **142**, 1933–1940.
18 K. Zhao, W. Zhu, S. Liu, X. Wei, G. Ye, Y. Su and Z. He, *Nanoscale Adv*, 2020, **2**, 536–562.
19 M. Yu, R. Dong and X. Feng, *J Am Chem Soc*, 2020, **142**, 12903–12915.
20 H. Zhong, M. Wang, G. Chen, R. Dong and X. Feng, *ACS Nano*, 2022, **16**, 1759–1780.
21 H. Zhong, K. H. Ly, M. Wang, Y. Krupskaya, X. Han, J. Zhang, J. Zhang, V. Kataev, B. Büchner, I. M. Weidinger, S. Kaskel, P. Liu, M. Chen, R. Dong and X. Feng, *Angewandte Chemie - International Edition*, 2019, **58**, 10677–10682.
22 J. Liu, D. Zhu, C. X. Guo, A. Vasileff and S. Qiao, *Adv Energy Mater*.
23 P. Kielb, M. Horch, P. Wrzolek, R. Goetz, K. H. Ly, J. Kozuch, M. Schwalbe and I. M. Weidinger, *Catal Sci Technol*, 2018, **8**, 1849–1857.
24 H. K. Ly, P. Wrzolek, N. Heidary, R. Götz, M. Horch, J. Kozuch, M. Schwalbe and I. M. Weidinger, *Chem Sci*, 2015, **6**, 6999–7007.
25 K. H. Ly and I. M. Weidinger, *Chemical Communications*, 2021, **57**, 2328–2342.
26 N. Heidary, D. Chartrand, A. Guiet and N. Kornienko, *Chem Sci*, 2021, **12**, 7324–7333.
27 A. Alsudairi, J. Li, N. Ramaswamy, S. Mukerjee, K. M. Abraham and Q. Jia, *J Phys Chem Lett*, 2017, **8**, 2881–2886.
28 Z. Chen, S. Jiang, G. Kang, D. Nguyen, G. C. Schatz and R. P. van Duyne, *J Am Chem Soc*, 2019, **141**, 15684–15692.
29 J. Wei, D. Xia, Y. Wei, X. Zhu, J. Li and L. Gan, *ACS Catal*, 2022, **12**, 7811–7820.
30 Z. Wang, L. S. Walter, M. Wang, P. S. Petkov, B. Liang, H. Qi, N. N. Nguyen, M. Hambsch, H. Zhong, M. Wang, S. Park, L. Renn, K. Watanabe, T. Taniguchi, S. C. B. Mannsfeld, T. Heine, U. Kaiser, S. Zhou, R. T. Weitz, X. Feng and R. Dong, *J Am Chem Soc*, 2021, **143**, 13624–13632.
31 Z. Wang, D. Liu, H. Gu, A. Zhu, Y. Tian and G. Shi, *Biosens Bioelectron*, 2013, **43**, 101–107.
32 T. Sun, Y. Li, T. Cui, L. Xu, Y. G. Wang, W. Chen, P. Zhang, T. Zheng, X. Fu, S. Zhang, Z. Zhang, D. Wang and Y. Li, *Nano Lett*, 2020, **20**, 6206–6214.
33 G. Kresse and J. Furthmüller, *Comput Mater Sci*, 1996, **6**, 15–50.
34 G. Kresse and D. Joubert, *Phys Rev B*, 1999, **59**, 1758–1775.
35 J. P. Perdew, K. Burke and M. Ernzerhof, *Phys Rev Lett*, 1996, **77**, 3865–3868.
36 S. Grimme, *J Comput Chem*, 2006, **27**, 1787–1799.
37 V. I. Anisimov, F. Aryasetiawan and A. I. Lichtenstein, *J. Phys.: Condens. Matter*, 1997, **9**, 767.
38 W. Li, L. Sun, J. Qi, P. Jarillo-Herrero, M. Dincă and J. Li, *Chem Sci*, 2017, **8**, 2859–2867.
39 H. J. Monkhorst and J. D. Pack, *Phys Rev B*, 1976, **13**, 5188–5192.
40 R. Dovesi, A. Erba, R. Orlando, C. M. Zicovich-Wilson, B. Civalleri, L. Maschio, M. Rérat, S. Casassa, J. Baima, S. Salustro and B. Kirtman, *WIREs Computational Molecular Science*, 2018, **8**, e1360.
41 R. Dovesi, V. Saunders, C. Roetti, R. Orlando, C. M. Zicovich-Wilson, F. Pascale, B. Civalleri, K. Doll, N. Harrison, I. Bush, M. Llunel, M. Causà, Y. Noël, L. Maschio, A. Erba, M. Rérat and S. Casassa, *CRYSTAL17 User's Manual*, 2018.
42 C. Adamo and V. Barone, *Journal of Chemical Physics*, 1999, **110**, 6158–6170.
43 S. Grimme, J. Antony, S. Ehrlich and H. Krieg, *J Chem Phys*, 2010, **132**, 154104.
44 J. Heyd, G. E. Scuseria and M. Ernzerhof, *Journal of Chemical Physics*, 2003, **118**, 8207–8215.
45 M. F. Peintinger, D. V. Oliveira and T. Bredow, *J Comput Chem*, 2013, **34**, 451–459.